HHS Public Access

Author manuscript

Microfluid Nanofluidics. Author manuscript; available in PMC 2016 October 17.

Published in final edited form as:

Microfluid Nanofluidics. 2016 ; 20(2): . doi:10.1007/s10404-016-1707-4.

Design of microfluidic channels for magnetic separation of malaria-infected red blood cells

Wei-Tao Wu[1], **Andrea Blue Martin**[1], **Alberto Gandini**[1], **Nadine Aubry**[2], **Mehrdad Massoudi**[3], and **James F. Antaki**[1]

Mehrdad Massoudi: MASSOUDI@NETL.DOE.GOV

[1]Department of Biomedical Engineering, Carnegie Mellon University, Pittsburgh, PA, 15213, USA

[2]Department of Mechanical Engineering, Northeastern University, Boston, MA, 02115, USA

[3]U. S. Department of Energy, National Energy Technology Laboratory (NETL), PA, 15236, USA

Abstract

This study is motivated by the development of a blood cell filtration device for removal of malaria-infected, parasitized red blood cells (pRBCs). The blood was modeled as a multi-component fluid using the computational fluid dynamics discrete element method (CFD-DEM), wherein plasma was treated as a Newtonian fluid and the red blood cells (RBCs) were modeled as soft-sphere solid particles which move under the influence of drag, collisions with other RBCs, and a magnetic force. The CFD-DEM model was first validated by a comparison with experimental data from Han et al. 2006 (Han and Frazier 2006) involving a microfluidic magnetophoretic separator for paramagnetic deoxygenated blood cells. The computational model was then applied to a parametric study of a parallel-plate separator having hematocrit of 40% with a 10% of the RBCs as pRBCs. Specifically, we investigated the hypothesis of introducing an upstream constriction to the channel to divert the magnetic cells within the near-wall layer where the magnetic force is greatest. Simulations compared the efficacy of various geometries upon the stratification efficiency of the pRBCs. For a channel with nominal height of 100 μm, the addition of an upstream constriction of 80% improved the proportion of pRBCs retained adjacent to the magnetic wall (separation efficiency) by almost 2 fold, from 26% to 49%. Further addition of a downstream diffuser reduced remixing, hence improved separation efficiency to 72%. The constriction introduced a greater pressure drop (from 17 to 495 Pa), which should be considered when scaling-up this design for a clinical-sized system. Overall, the advantages of this design include its ability to accommodate physiological hematocrit and high throughput – which is critical for clinical implementation as a blood-filtration system.

Keywords

Blood; malaria; microchannels; magnetic field; cell separation

Address for correspondence: James F. Antaki, PhD, Carnegie Mellon University, 700 Technology Dr, Pittsburgh, PA 15219. Phone: 412-268-9857. antaki@cmu.edu.

INTRODUCTION

Malaria afflicts 300 to 500 million people worldwide and consumes 40% of the health expenditures of over 100 countries. The World Health Organization (WHO) estimates nearly one million deaths annually, 85% of which are children under five years of age (WHO 2013). It has been known for many decades that the malaria-infected, parasitized RBCs (pRBCs) exhibit paramagnetic properties; therefore it is possible to separate and remove the pRBCs by applying a force via a high magnetic field gradient (Paul et al. 1981; Zborowski et al. 2003; Moore et al. 2006; Hackett et al. 2009). This has motivated the development of a magnetic apheresis (mPharesis™) system to continuously purify a patient's blood, much like a dialyzer (Kim et al. 2012; Gandini et al. 2013) (see Fig. 1). The unique challenge of this application is its ability to target ring-stage pRBCs, which have a relatively weak magnetic susceptibility, and the need for high-throughput on the order of 100mL/min – similar to standard hemodialysis.

The mPharesis™ filter design includes a stack of laminar flow microchannels through which the infected blood is transported and exposed to a high magnetic field gradient (>1000 T/m) created by an array of ferromagnetic wires embedded on one wall of the channel. (See Fig. 1, bottom.) This causes the pRBCs to migrate or "marginate" towards the wall towards the source of the magnetic force whereupon they can be skimmed off by a side branch (bleed-slit) downstream. The purified blood is then returned to the patient. The engineering challenge is to optimize the efficiency of this magnetophoretic separator to maintain the overall size of the system within the desired envelope and limit the treatment time under 4 hours. (Kim et al. 2012)

This present numerical study focused on the influence of the geometry of an individual separation channel of the mPharesis™ device on the efficiency of magnetic separation. Specifically, it explored the hypothesis that the introduction of a constriction at the entrance of the channel would improve the efficiency compared to a standard parallel-plate channel. The assumption was that since the magnetic force diminishes very rapidly with distance from the magnet poles, it would be advantageous to initially divert the magnetic cells in close proximity to the greatest force where they would be retained by the magnetic force. Downstream of the constriction, the non-magnetic healthy cells would diffuse across the height of the channel, while the magnetic cells would remain close to the wall. An added diffuser is introduced to further streamline the flow and improve the separation.

METHODS

Numerical simulations were performed with two computational domains, depicted in Fig. 2 and Fig. 3. Fig. 2 depicts a 3-way magnetophoretic separator in a previously reported experiment by Han et al. (Han and Frazier 2006) which was used for validation of the computational model described here. For economy of computational cost, a symmetry condition was assumed, reducing the domain to half the width (see Fig. 2(b)). Fig. 3 represents a single separation channel of the mPharesis™ device (not drawn to scale). In both devices, blood flows within the channel along the positive × direction. A magnetic gradient is generated by an external uniform magnetic field, provided by a permanent

magnet (not shown) in proximity with a ferromagnetic wire. The solutions to the equations of motion were solved using computational fluid dynamics discrete element method (CFD-DEM). This was chosen as a reasonable alternative to mesoscale simulations, like the Lattice Boltzman and/or Immersed Boundary Methods, but with more economical computational cost. The details of the constitutive models and numerical methods are provided below.

Governing Equations for Blood Flow

Blood was treated as a multi-component system, comprised of RBCs and plasma. White cells are considered too dilute to affect the flow system. The plasma was treated as a Newtonian fluid, obeying the following conservation of mass,

$$\frac{\partial \rho_p}{\partial t} + \mathrm{div}(\rho_p \boldsymbol{v}_p) = 0 \quad (1)$$

where $\frac{\partial}{\partial t}$ is the derivative with respect to time, *div* is the divergence operator, $\rho_p = \varepsilon\rho_{p0}$, is the density of plasma, ρ_{p0} is the density of the plasma in the reference configuration, ε is the volume fraction of plasma (1-hematocrit), and $\boldsymbol{v_p}$ is the velocity field. ε in turn is computed using the method introduced by Link et al. (Link et al. 2005). The corresponding balance of linear momentum is:

$$\rho_p \frac{D^p \boldsymbol{v}_p}{Dt} = \mathrm{div}(\boldsymbol{T}_p) + \rho_p \boldsymbol{b}_p + \boldsymbol{F}_{\mathrm{pr}} \quad (2)$$

where $\boldsymbol{T}_p = [-\varepsilon p + \varepsilon\lambda_p tr\boldsymbol{D}_p]\boldsymbol{I} + 2\mu_p$, p is the pressure of the mixture, λ_p and μ_p are the (constant) first and second coefficients of viscosity of the pure plasma, where $\boldsymbol{D}_p = \frac{1}{2}[(\mathrm{grad}\ \boldsymbol{v}_p) + (\mathrm{grad}\ \boldsymbol{v}_p)^T]$. In general for any scalar β, $\frac{D^\alpha \beta}{Dt} = \frac{\partial \beta}{\partial t} + \boldsymbol{v}^\alpha \cdot \nabla\beta$, $\alpha = f, s$, and (for any vector $\boldsymbol{w}$), $\frac{D^\alpha \boldsymbol{w}}{Dt} = \frac{\partial \boldsymbol{w}}{\partial t} + (\nabla \boldsymbol{w})\boldsymbol{v}^\alpha$, $\boldsymbol{T}_p$ represents the Cauchy stress tensors, $\boldsymbol{F}_{pr}$ represents the interaction forces (exchange of momentum) between the plasma and RBCs (more detail see Johnson et al., 1990 and Wu et al., 2014), and $\boldsymbol{b}_p$ refers to the body force. The balance of the angular momentum implies that, in the absence of couple stresses, the total Cauchy stress tensor is symmetric.

The equation of motion of the RBC component is represented in a similar fashion:

$$m_r \frac{D^2 \boldsymbol{x}_r}{Dt} = \boldsymbol{F}_{\mathrm{contact}} + \boldsymbol{F}_{\mathrm{pr}} + \boldsymbol{F}_{\mathrm{ext}} \quad (3)$$

where m_r is the mass of a RBC, $\boldsymbol{x}_r$ is the instantial space position of RBCs, $\boldsymbol{F}_{contact}$ is the force of collision with other RBCs or boundaries, $\boldsymbol{F}_{pr}$ is the interaction force with continuous phase (plasma) and $\boldsymbol{F}_{ext}$ is the external force field, in this case the magnetic

force. In current study, $\boldsymbol{F}_{pr}$ includes only the drag force, and is represented by the drag model of Rusche and Issa (Rusche and Issa 2000).

RBCs collision: Soft-sphere model

The soft-sphere model incorporates multiple particle-particle interactions with the trajectories determined by integrating Newton's second law. According to Cundall and Strack (Cundall and Strack 1979), the normal component of the contact force, $\boldsymbol{F}_{\text{contact}}^{m,n}$, acting on particle i by particle j (or wall) is,

$$\hat{\boldsymbol{F}}_{\text{contact}}^{m,n} = -\hat{k}\delta\boldsymbol{n}^{m,n} - \hat{\eta}\boldsymbol{v}_r^{m,n} \quad (4)$$

Where $\hat{k}$ and $\hat{\eta}$ are the normal "spring" stiffness and damping coefficient respectively, $\delta = (R_m + R_n) - |\boldsymbol{r}_m - \boldsymbol{r}_n|$ is a (fictitious) overlap between two RBCs, R is the radius of a RBC, $\boldsymbol{n}^{m,n} = (\boldsymbol{r}_m - \boldsymbol{r}_n)/|\boldsymbol{r}_m - \boldsymbol{r}_n|$ is the normal unit vector between two RBCs, $\boldsymbol{v}_r^{m,n} = (\boldsymbol{v}_m - \boldsymbol{v}_n) + (R_m\boldsymbol{\omega}_m + R_n\boldsymbol{\omega}_n) \times \boldsymbol{n}^{m,n}$ is the relative velocity, $\hat{\boldsymbol{v}}_r^{m,n} = (\boldsymbol{v}_r^{m,n}.\boldsymbol{n}^{m,n})\boldsymbol{n}^{m,n}$ is the *normal* relative velocity, and $\boldsymbol{\omega}$ is the angular velocity. The tangential component of the contact force between particles is likewise:

$$\tilde{\boldsymbol{F}}_{\text{contact}}^{m,n} = \begin{cases} -\tilde{k}\tilde{\delta} - \tilde{\eta}\tilde{\boldsymbol{v}}_r^{m,n} \text{ for } |\tilde{\boldsymbol{F}}_{\text{contact}}^{m,n}| \le \mu_f|\hat{\boldsymbol{F}}_{\text{contact}}^{m,n}| \\ -\mu_f\left||\hat{\boldsymbol{F}}_{\text{contact}}^{m,n}|\right|\boldsymbol{t}^{m,n} \text{ for } |\tilde{\boldsymbol{F}}_{\text{contact}}^{m,n}| > \mu_f|\hat{\boldsymbol{F}}_{\text{contact}}^{m,n}| \end{cases} \quad (5)$$

where $\hat{k}$, $\hat{\eta}$, and μ_f are the tangential spring stiffness, tangential damping coefficient, and friction coefficient, respectively, $\tilde{\boldsymbol{v}}_r^{m,n} = \boldsymbol{v}_r^{m,n} - \hat{\boldsymbol{v}}_r^{m,n}$ is the relative tangential velocity.

The tangential displacement $\tilde{\delta}$ is given by:

$$\tilde{\delta} = \begin{cases} \hat{\delta}_0\boldsymbol{H} + \int_{\text{to}}^{t}\tilde{\boldsymbol{v}}_r^{m,n}dt \text{ for } |\tilde{\boldsymbol{F}}_{\text{contact}}^{m,n}| \le \mu_f|\hat{\boldsymbol{F}}_{\text{contact}}^{m,n}| \\ -\mu_f|\hat{\boldsymbol{F}}_{\text{contact}}^{m,n}|\boldsymbol{t}^{m,n}/k_t \text{ for } |\tilde{\boldsymbol{F}}_{\text{contact}}^{m,n}| > \mu_f|\hat{\boldsymbol{F}}_{\text{contact}}^{m,n}| \end{cases} \quad (6)$$

$$\boldsymbol{H} = \begin{bmatrix} qh_x^2 + c & qh_xh_y - sh_z & qh_xh_z + sh_y \\ qh_xh_y + sh_z & qh_y^2 + c & qh_yh_z - sh_x \\ qh_xh_z - sh_y & qh_yh_z + sh_x & qh_z^2 + c \end{bmatrix} \quad (7)$$

Where, $\boldsymbol{t}^{m,n} = \tilde{\boldsymbol{v}}_r^{m,n}/|\tilde{\boldsymbol{v}}_r^{m,n}|$ is the tangential unit vector, $\boldsymbol{h} = (\boldsymbol{n}^{m,n} \times \boldsymbol{n}_0^{m.n})/|\boldsymbol{n}^{m,n} \times \boldsymbol{n}_0^{m.n}|$, $c = \cos\varphi$, $s = \sin\varphi$, $q = 1 - c$, $\varphi = \arcsin|\boldsymbol{n}^{m.n} \times \boldsymbol{n}_0^{m.n}|$, $\hat{\delta}_0$ and $\boldsymbol{n}_0^{m.n}$ are the tangential displacement and normal direction in the previous time step, respectively and μ_f is the frictional coefficient. The mechanism of the particle-wall collision is same to the particle-particle collision. (For further details of the derivation, the reader is referred to Su et al.,

2011 and van der Hoef et al., 2006. The determination of the stiffness and damping coefficient can be found in Tsuji et al., 1992 or van der Hoef, 2006.

Magnetic Field

According to Han et al. (Han and Frazier 2004; Han and Frazier 2006), the expression for the magnetic force produced by a magnetically saturated, ferromagnetic rectangular wire placed under a uniform external magnetic field referenced to a coordinate system centered at the origin as shown in Fig. 2 is:

$$\boldsymbol{F}_{\text{magnetic}}(z',y')=\mu_0 M_s(\chi_{rbc}-\chi_p)V_{rbc}a^2H_0\frac{\left(\frac{M_s}{2H_0}a^2+3(a+y')^2-z'^2\right)z'}{\left(z'^2+(a+y')^2\right)^3}\boldsymbol{e}_{z'}$$
$$+\mu_0 M_s(\chi_{rbc}-\chi_p)V_{rbc}a^2H_0\frac{\left(\frac{M_s}{2H_0}a^2-3z'^2+(a+y')^2\right)(a+y')}{\left(z'^2+(a+y')^2\right)^3}\boldsymbol{e}_{y'} \quad (8)$$

where $\mathbf{e_z}$, and $\mathbf{e_y}$, are the unit vectors in the z' and y' directions, respectively, and $y' \geq 0$; $k=\frac{\mu_w-\mu_0}{\mu_w+\mu_0}=1$ here, μ_w and μ_0 are the magnetic permeability of the ferromagnetic wire and free space, respectively; M_s is the saturation magnetization field of the rectangular wire; χ_p and χ_{rbc} are the magnetic susceptibilities of the plasma and the RBCs; V_{rbc} is the volume of the RBCs; and a is the nominal radius of the wire, which for a rectangular wire is half of the wire height, 25 μm; H_0 is the applied external magnetic field. The above governing equations were implemented in OpenFOAM (OpenCFD 2011), and solved on a PC workstation (Dell T7910). The mesh dependency studies were performed and discussed in detail in the channel optimization part of the results section. All the symbols used in current paper are summarized in the Appendix.

RESULTS

Computational Model Validation: deoxyhemoglobin RBCs separation

Simulations of the magnetophoretic microfluidic separator used by Han et al. (Han and Frazier 2004; Han and Frazier 2006) were performed for four flow rates, corresponding to average velocity of 0.1, 0.2, 0.4 and 0.6 mm/s. The Re is about 0.0094 for the inlet velocity of 0.1 mm/s and the apparent kinematic viscosity of plasma was $0.94e^{-6}$ m^2/s. The hematocrit was assumed to be 4%, based on the reported dilution of bovine whole blood of 1:10 (Han and Frazier 2006), and assuming a nominal hematocrit of bovine whole blood as 44% (Oshima and Sankai 2009). Additional physical parameters are provided in Table 1. The initial condition for all the simulations were a cell-free domain. A uniform inlet boundary condition was applied. All simulations were run for a duration of 5× (length of the channel/mean velocity) to assure steady state conditions. For economy of computational cost, all simulations were performed in 2-D on x-y plane at z=0, with coordinates shown in Fig. 2 and assumed symmetric geometry however, the geometries replicate the salient features. Accordingly, the inlet velocity boundary condition was assumed to be 1.5 times the

average velocity, to correspond with the centerline velocity. The magnetic field was prescribed by equation (8) with z=0 corresponding to the centerline of the channel:

$$\boldsymbol{F}_{\text{magnctic}}(y')=\mu_0 M_s(\chi_{rbc}-\chi_p)V_{rbc}a^2H_0\frac{\left(\frac{M_s}{2H_0}a^2+(a+y')^2\right)}{(a+y')^5}\boldsymbol{e}_{y'} \quad (9)$$

Fig. 4 shows the distribution of paramagnetic deoxyhemoglobin RBCs passing through the separator near the outlet region. It can be seen that both simulations and experiments that the applied magnetic force has an obvious effect on the distribution of RBCs. (The simulation appears less dense because it is two-dimensional.) Fig. 5 compares the simulated versus measured percentage of RBCs exiting the central outlet (outlet2 in Fig. 2) for the four velocities considered as well as the control case in which there is no magnet. There was a small systematic over-prediction of RBC percentage by simulation of 0.8%–4.7%, which was observed to be a function of flow rate.

Channel Optimization for Separation of Malaria Infected RBCs

Based on the excellent agreement between the numerical and experimental results in the above case, the CFD-DEM model was applied to a parametric study of the mPharesis separation channel. Some of the conditions were adjusted to correspond to the realistic application of the device clinically. In particular, the hematocrit was prescribed as 40%, with a ratio of malaria-infected, parasitized RBCs (pRBCs) to healthy RBCs of 1:9. Also, the magnetic susceptibility difference between the pRBCs ($\chi_{\text{pRBC}} = -6.2e^{-6}$) and plasma was prescribed as $1.5e^{-6}$ (SI units), corresponding to ring-stage malaria (Hackett et al. 2009; Kim et al. 2012), approximately 2.5× less than deoxyhemoglobin RBCs ($\chi_{\text{deoxyRBC}} = -3.8e^{-6}$) used in the Han et al.'s experiment. All simulations were performed in 2-D to economize computational costs, similar to the previous simulation. Furthermore the domain was limited to the middle region of the channel, which excluded entrance effects and the bleed slit, as shown in Fig. 3. The computed magnitude of the magnetic force was found to decay very quickly with distance from the wire, resulting in significantly less force (<1%) at the far wall (y=H) than the near wall (see Fig. 3). However, these cells near the far wall have the farthest to travel to completely stratify the blood. For this reason, we introduce an upstream constriction, shown Fig. 3(b), to initially bring all cells in close proximity to the greatest magnetic force. Thereafter, when the channel expands to its full height the uninfected RBCs can transport away from the magnetic wall leaving the pRBCs trapped in a boundary layer. An added diffuser is introduced to streamline the flow downstream of the constriction (see Fig. 3(c)). Without loss of generality, the length of the channels was all specified as 10 mm.

The inlet velocity for all the cases was set as 1.0 mm/s, corresponding to Re=0.057 based on an apparent kinematic viscosity of whole blood as $3.32e^{-6}$ m^2/s. All simulations were run for a duration of 5× (length of the channel/mean velocity) to assure steady state conditions were reached. To account for the discretization of the pRBCs and RBCS phases, all data shown in the following sections are averaged from 100 different time steps. Prior to simulations of the various geometries of the channels, a mesh dependency study was first

performed using the 10 mm-length rectangular channel (see Fig. 3(a)). It was found that meshes of 18288 and 31248 nodes both closely approximated the theoretical (Newtonian) prediction, therefore a mesh with 18288 nodes was chosen. Mesh dependency studies were confirmed for the other geometries as well.

For quantifying the separation efficiency, the pRBCs density distribution across the channel was evaluated at the outlet. To accommodate the discrete size of the cells, the outlet was discretized into 20 regions, each 5 μm in height. Although the bleed slit was not included in the simulation, the presumption was that the flow exiting the outlet would be split such that the concentrated pRBCs layer of blood would be collected, and the remaining blood returned to the patient. The specific split ratio would be chosen based on clinical considerations, such as availability of blood, risk of anemia, etc.

Effect of Constriction Height, H_c (L_c=2 mm)—The pRBCs distributions are provided in Fig. 6 for rectangular constrictions of 50% and 80%, 2 mm in length, and are compared with the baseline (no constriction). Table 2 shows the percentage of the pRBCs in the near-wall subzone (20 μm). We defined two metrics to assess the degree of separation. The first was simply the relative quantity of pRBCs captured within the 20 μm subzone at the outlet:

$$\text{pRBC Capture\%}=\frac{\text{pRBCs near wall}}{\text{total pRBCs}}$$

A value of 20% (percent of RBCs that are infected pRBCs) would imply no stratification of pRBCs, and 100% would correspond to complete stratification. A second index, *pRBC enrichment* describes the relative increase in concentration of pRBCs in the sub-layer compared to the bulk,

$$\text{pRBC enrichment}=\frac{\text{pRBCs concentration near wall}}{\text{bulk pRBCs concentration}}-1 \quad (10)$$

The above index ranges from 0% for no stratification to a maximum of 400% if all cells are stratified to the sub-layer (i.e. pRBC concentration from 4% to 16%).

As contrasted to the channel without constriction, which provided very limited enrichment (28%) the channels with constrictions were markedly more efficient (91.5% and 139% for the 50 μm and 20 μm constriction respectively.)

Effect of Constriction Length L_c (H_c=80%)—To evaluate the relative benefit of lengthening the constriction L_c, six (different lengths were evaluated (0.2, 0.5, 1.0, 2.0, 4.0 and 8.0 mm) each having a height of 20 μm. These results are provided in Fig. 7 and Table 3. It can be seen that there is a slight improvement with length from 0.2 mm up to 4 mm, beyond which further extension to 8 mm yields diminishing returns.

Effect of the diffuser after the constriction L_d (L_c=2 mm, H_c=80%)—Following the constriction, it is desired for the RBCs to gradually advect from the wall, leaving the

pRBCs trapped in the magnetic boundary layer. However a sudden expansion was observed to cause a flow disturbance that draws pRBCs away from the wall. (See Fig. 8(a).) Therefore a tapered diffuser was introduced for the case of 80 μm × 2 mm constriction. (See Fig. 8(b).) The corresponding concentration profiles at the exit of the channel are provided in Fig. 9 and Table 4 which reveals a dramatic improvement (from 139% to 261%) by introducing a diffuser of just 1 mm. The incremental improvement by extending the diffuser to 2 mm was negligible.

DISCUSSION

Many groups over the past decades have proposed unique microfluidic geometries designed to improve the magnetic separation of cells (Melville et al. 1975; Kumar and Lykke 1984; Zborowski et al. 1999), particles (Gerber 1984; Lien et al. 2007; Wu et al. 2011; Zhu et al. 2011; Verbruggen et al. 2015) and other suspensions. A common practice involves attaching magnetic particles to target cells, proteins, fungi, or viruses to improve separation efficiency (Hayes et al. 2001; Furdui and Harrison 2004; Inglis et al. 2004; Kim and Park 2005; Pamme et al. 2006; Xia et al. 2006; Chen et al. 2007; Hahn et al. 2007; Earhart et al. 2009; Yung et al. 2009; Kang et al. 2012). High magnetic gradient microfluidic separators involving RBCs and pRBCs have been published using an external permanent magnet (Chikov et al. 1993; Karl et al. 2008), external magnets in combination with ferromagnetic bead or steel wool packed columns (Owen 1978; Fairlamb et al. 1984; Nalbandian et al. 1995; Ahn et al. 1996; Carter et al. 2003; Trang et al. 2004; Ribaut et al. 2008; Karl et al. 2009; Bhakdi et al. 2010), embedded ferromagnetic elements (Melville et al. 1975; Paul et al. 1981; Takayasu et al. 1982; Han and Frazier 2006; Furlani 2007; Iliescu et al. 2009), and/or saline buffer clearance streams (Nam et al. 2013). Although high separation efficiencies have been reported, none of these separators are practical for a continuous, high-throughput blood purification system to treat a malaria-infected patient. Batch devices can collect only small quantities at a time and must either be repeatedly replaced or purged. Reported continuous systems require highly diluted blood (e.g. <5% hematocrit), and sometimes the addition of a sheath fluid layer, to efficiently capture the target cells. In both cases, it would be necessary to re-concentrate the blood prior to returning it to the patient. Furthermore, very few studies attempted the separation of ring-stage malaria-infected cells with only one showing significant success, though with a low throughput (73% separation efficiency at approximately 200–300 pRBCs per minute) (Nam et al. 2013). Most high gradient magnetic separators target ferromagnetic particles, which are 1000× or more paramagnetic than mature pRBCs, or often deoxygenated RBCs which are 2.5× more paramagnetic. Unlike these other separators, the mPharesis design is also capable of capturing immature ring-stage pRBCs with its novel, parametrically optimized magnetic force field. The parallel-plate type geometry reported here is attractive for treating severe malaria as it offers the possibility of selectively removing weakly-magnetic infected cells without wasting healthy cells or diluting the filtered blood. It is also more amenable for up-scaling because it can be extended in the width direction, and can be stacked in layers.

The rapid decay of the magnetic force with distance restricts the range over which it can attract and maintain malaria-infected cells to within a few tens of microns. The hypothesis of improved pRBC separation efficiency with the introduction of an upstream constriction was

confirmed with parametric optimization. The constriction diverted the flow within 20–50 μm of the magnetic wall and, upon exiting the constriction, retained the pRBCs near while the non-magnetic RBCs would diffuse back into the bulk flow. The addition of a short diffuser allowed the separation to occur more gradually, avoiding re-mixing and resulting in markedly improved separation efficiency. It was observed that the length of the constriction need not be very long, which is fortuitous as it limits its effect on pressure drop. For example the performance of a 1 mm long constriction was comparable to 2 mm yet exhibited approximately half the pressure drop.

The CFD-DEM method applied in this study was advantageous inasmuch as it allowed discrimination between pRBCs and healthy RBCs. Several approaches were considered for current problem, including multi-components Eulerian model, CFD-DEM model, and mesoscale simulation such as Immersed Boundary Method combined with the Lattice Boltzmann Method (LBM-IBM) (Zhang et al. 2008; Fenech et al. 2009; Yin et al. 2013; Wu et al. 2014b; Wu et al. 2015). The limitation with the multi-components Eulerian model, however is the necessity to identify the interaction forces between pRBCs and RBCs, which is not currently known. Also computational cost of applying LBM-IBM method would be prohibitively expensive, considering that the number of the particles in the system is about 0 (10^5).

The size of the problem also poses numerical challenges for the general CFD-DEM method. Usually when the CFD mesh contains 0 (10^2) particles, the volume fraction of the fluid can be directly calculated as proposed by Hoomans et al. (Hoomans et al. 1996), however when the size of the particle is in the same order of the CFD mesh this method may cause numerical instability. Therefore, in current study the volume fraction of RBCs, ϕ, was computed using the method introduced by Link et al. (Link et al. 2005). Another limitation relates to necessary assumptions regarding the interaction forces, and specifically the drag forces on the cells. In this study, we did not explicitly model the biconcave geometry of the red blood cell; however the model does not have any provision for cell shape, but rather accounts for the presence of cells mathematically in terms of their drag force and collision force. Excellent numerical replication of Han's experimental data confirmed the applicability of our implementation of CFD-DEM approach to the problem of RBCs separation using magnetic force (Han and Frazier 2006).

Although the optimized channel yielded much better separation efficiency compared to baseline, it is still far from perfect: capturing up to 73% of the pRBCs in the near-wall layer versus 100% if the separator was able to stratify *all* the pRBCs. Furthermore, the above capture index is based on the presumption that 20% of the channel height is skimmed off into a waste slit or branch; which would also imply that a significant proportion of healthy cells would be discarded as well. Therefore, for the current case of 1:9 pRBC/RBC with 40% hematocrit, the *ideal* device would concentrate all the infected cells within a 4 μm skimming layer. Although this is not a likely prospect, as this would restrict the pRBCs to a monolayer adjacent to the magnetic wall, it is evident from comparison of Fig. 8(a) to Fig. 8(b), that the degree of re-mixing can be mitigated by replacing a sudden expansion with a gradual diffuser. Therefore there is an opportunity to improve the stratification efficiency if the upward forces acting on these cells (i.e. lift, drag, and collisions with RBCs) could be

reduced, for example by additional shape optimization, both in the height and width of the channel (y and z dimensions).

Although this optimization was performed in the context of a specific parallel-plate geometry, the results may be applicable to any magnetophoretic separator geometry with a single ferromagnetic pole or array of poles. For example, continuous microfluidic high gradient magnetic separators such as Han et al. 2006, Nam et al. 2013, and Furlani et al. 2007 could potentially be improved by introducing a constriction and diffuser as reported here. (Han and Frazier 2006; Furlani 2007; Nam et al. 2013) Additionally, experimental results could be extrapolated to target cells with different magnetic susceptibilities by appropriately scaling the flow conditions. We illustrated this by performing an additional simulation to consider an earlier stage of the RBC portion of the malaria infection (ring-stage) in which the magnetic susceptibility is reduced by 1/3 from 1.5 to $0.5e^{-6}$ (SI) corresponding to approximately 10–15 h after parasite invasion. The best performing channel (H_c = 80 μm, L_c = 2 mm, and L_d = 2 mm) was processed with a proportionately decreased inlet velocity (from 1.0 to 0.33 mm/s) and the resultant capture rate and pRBC enrichment were 66% and 232% respectively, which is comparable to the results shown in the previous section.

CONCLUSIONS

Magnetic separation of parasitized, malaria-infected red blood cells within a parallel plate system was simulated using a CFD-DEM (Eulerian-Lagrangian) approach. The plasma was treated as a Newtonian fluid (as the Eulerian phase), and the RBCs were treated as soft spheres (as the Lagrangian phase) influenced by drag, collisions with other RBCs and a magnetic field. The CFD-DEM approach was shown to accurately predict previously reported experimental observations by Han et al. Using this model, we determined that the introduction of a constriction and diffuser into an otherwise parallel-plate channel was effective for improving the retention of the paramagnetic cells within the magnetic force, and hence the overall separation efficiency. For the cases studied, it was found that a constriction of 50 μm in height, 2 mm in length followed by a 2 mm diffuser performed almost as well as a narrower and longer constriction of 20 μm × 8 mm, suggesting that a subtle modification to the blood flow channel can provide a profound beneficial effect. The constriction introduced a greater pressure drop (from 17 to 495 Pa), which should be considered when scaling-up this design for a clinical-sized device. The ability to accommodate physiological hematocrit and high throughput motivate further consideration for translation to a treatment-scale device.

Acknowledgments

This research was supported by NIH grant 1 R01 HL089456.

REFERENCES

Ahn CH, Allen MG, Trimmer W, et al. A fully integrated micromachined magnetic particle separator. J Microelectromechanical Syst. 1996; 5:151–158.

Bhakdi SC, Ottinger A, Somsri S, et al. Optimized high gradient magnetic separation for isolation of Plasmodium-infected red blood cells. Malar J. 2010; 9:38. [PubMed: 20122252]

Carter V, Cable HC, Underhill BA, et al. Density Gradient Columns and Magnetic Isolation. Malar J. 2003; 6:1–6.

Chen H, Bockenfeld D, Rempfer D, et al. Three-dimensional modeling of a portable medical device for magnetic separation of particles from biological fluids. Phys Med Biol. 2007; 52:5205–18. [PubMed: 17762081]

Chikov V, Kuznetsov A, S A. Single cell magnetophoresis and its diagnostic value. J Magn Magn Mater. 1993; 122122:367–370.

Cundall PA, Strack ODL. A Discrete Numerical Model for Granular Assemblies. Geotechnique. 1979; 29:47–65.

Dean D, Hemmer J, Vertegel A, Laberge M. Frictional Behavior of Individual Vascular Smooth Muscle Cells Assessed By Lateral Force Microscopy. Materials (Basel). 2010; 3:4668–4680. [PubMed: 21686041]

Dulińska I, Targosz M, Strojny W, et al. Stiffness of normal and pathological erythrocytes studied by means of atomic force microscopy. J Biochem Biophys Methods. 2006; 66:1–11. [PubMed: 16443279]

Earhart CM, Wilson RJ, White RL, et al. Microfabricated magnetic sifter for high-throughput and high-gradient magnetic separation. J Magn Magn Mater. 2009; 321:1436–1439. [PubMed: 20161248]

Fairlamb AH, Paul F, Warhurst DC. A simple magnetic method for the purification of malarial pigment. Mol Biochem Parasitol. 1984; 12:307–312. [PubMed: 10610436]

Fenech M, Garcia D, Meiselman HJ, Cloutier G. A particle dynamic model of red blood cell aggregation kinetics. Ann Biomed Eng. 2009; 37:2299–2309. [PubMed: 19669883]

Furdui VI, Harrison DJ. Immunomagnetic T cell capture from blood for PCR analysis using microfluidic systems. Lab Chip. 2004; 4:614–618. [PubMed: 15570374]

Furlani EP. Magnetophoretic separation of blood cells at the microscale. J Phys D Appl Phys. 2007; 40:1313–1319.

Gandini A, Weinstein R, Sawh R, Parks D. Blood purification method and apparatus for the treatment of malaria. 2013

Gerber R. Magnetic filtration of ultra-fine particles. Magn IEEE Trans. 1984; 20:1159–1164.

Hackett S, Hamzah J, Davis TME, St Pierre TG. Magnetic susceptibility of iron in malaria-infected red blood cells. Biochim Biophys Acta (BBA)-Molecular Basis Dis. 2009; 1792:93–99.

Hahn YK, Jin Z, Kang JH, et al. Magnetophoretic immunoassay of allergen-specific IgE in an enhanced magnetic field gradient. Anal Chem. 2007; 79:2214–2220. [PubMed: 17288405]

Han K-H, Frazier AB. Paramagnetic capture mode magnetophoretic microseparator for high efficiency blood cell separations. Lab Chip. 2006; 6:265–273. [PubMed: 16450037]

Han K-H, Frazier AB. Continuous magnetophoretic separation of blood cells in microdevice format. J Appl Phys. 2004; 96:5797–5802.

Hayes MA, Polson NA, Phayre AN, Garcia AA. Flow-Based Microimmunoassay. Anal Chem. 2001; 73:5896–5902. [PubMed: 11791558]

Hoomans BPB, Kuipers JAM, Briels WJ, van Swaaij WPM. Discrete particle simulation of bubble and slug formation in a two-dimensional gas-fluidised bed: A hard-sphere approach. Chem Eng Sci. 1996; 51:99–118.

Iliescu C, Xu G, Barbarini E, et al. Microfluidic device for continuous magnetophoretic separation of white blood cells. Microsyst Technol. 2009; 15:1157–1162.

Inglis DW, Riehn R, Austin RH, Sturm JC. Continuous microfluidic immunomagnetic cell separation. Appl Phys Lett. 2004; 85:5093–5095.

Johnson, G.; Rajagopal, KR.; Massoudi, M. A review of interaction mechanisms in fluid-solid flows. PA (USA): USDOE Pittsburgh Energy Technology Center; 1990.

Kang JH, Krause S, Tobin H, et al. A combined micromagnetic-microfluidic device for rapid capture and culture of rare circulating tumor cells. Lab Chip. 2012; 12:2175. [PubMed: 22453808]

Karl S, David M, Moore L, et al. Enhanced detection of gametocytes by magnetic deposition microscopy predicts higher potential for Plasmodium falciparum transmission. Malar J. 2008; 7:66. [PubMed: 18439240]

Karl S, Davis TME, St-Pierre TG. A comparison of the sensitivities of detection of Plasmodium falciparum gametocytes by magnetic fractionation, thick blood film microscopy, and RT-PCR. Malar J. 2009; 8:98. [PubMed: 19432971]

Kim J, Massoudi M, Antaki JF, Gandini A. Removal of malaria-infected red blood cells using magnetic cell separators: A computational study. Appl Math Comput. 2012; 218:6841–6850. [PubMed: 22345827]

Kim KS, Park J-K. Magnetic force-based multiplexed immunoassay using superparamagnetic nanoparticles in microfluidic channel. Lab Chip. 2005; 5:657–664. [PubMed: 15915258]

Kumar RK, Lykke AWJ. Cell separation: a review. Pathology. 1984; 16:53–62. [PubMed: 6371684]

Lien K-Y, Lin J-L, Liu C-Y, et al. Purification and enrichment of virus samples utilizing magnetic beads on a microfluidic system. Lab Chip. 2007; 7:868–875. [PubMed: 17594006]

Link JM, Cuypers LA, Deen NG, Kuipers JAM. Flow regimes in a spout-fluid bed: A combined experimental and simulation study. Chem Eng Sci. 2005; 60:3425–3442.

Melville D, Paul F, Roath S. Direct magnetic separation of red cells from whole blood. 1975

Moore LR, Fujioka H, Williams PS, et al. Hemoglobin degradation in malaria-infected erythrocytes determined from live cell magnetophoresis. FASEB J. 2006; 20:747–749. [PubMed: 16461330]

Nalbandian RM, Sammons DW, Manley M, et al. A Molecular-based Magnet Test for Malaria. Am J Clin Pathol. 1995; 103:57–64. [PubMed: 7817946]

Nam J, Huang H, Lim H, et al. Magnetic separation of malaria-infected red blood cells in various developmental stages. Anal Chem. 2013; 85:7316–7323. [PubMed: 23815099]

OpenCFD. OpenFOAM Programmer's Guide Version 2.1.0. 2011

Oshima S, Sankai Y. Improvement of the accuracy in the optical hematocrit measurement by optimizing mean optical path length. Artif Organs. 2009; 33:749–756. [PubMed: 19775267]

Owen CS. High gradient magnetic separation of erythrocytes. Biophys J. 1978; 22:171–178. [PubMed: 656540]

Pamme N, Eijkel JCT, Manz A. On-chip free-flow magnetophoresis: Separation and detection of mixtures of magnetic particles in continuous flow. J Magn Magn Mater. 2006; 307:237–244.

Paul F, Roath S, Melville D, et al. Separation of malaria-infected erythrocytes from whole blood: use of a selective high-gradient magnetic separation technique. Lancet. 1981; 318:70–71.

Ribaut C, Berry A, Chevalley S, et al. Concentration and purification by magnetic separation of the erythrocytic stages of all human Plasmodium species. Malar J. 2008; 7:45. [PubMed: 18321384]

Rusche H, Issa RI. The Effect of Void age on the Drag Force on Particles, Droplets and Bubbles in Dispersed Two-Phase Flow. 2000

Su J, Gu Z, Xu XY. Discrete element simulation of particle flow in arbitrarily complex geometries. Chem Eng Sci. 2011; 66:6069–6088.

Takayasu M, Duske N, Ash SR, Friedlaender FJ. HGMS studies of blood cell behavior in plasma. IEEE Tr. 1982; 18:1520–1522.

Trang DTX, Huy NT, Kariu T, et al. One-step concentration of malarial parasite-infected red blood cells and removal of contaminating white blood cells. Malar J. 2004; 3:7. [PubMed: 15025790]

Tsuji Y, Tanaka T, Ishida T. Lagrangian numerical simulation of plug flow of cohesionless particles in a horizontal pipe. Powder Technol. 1992; 71:239–250.

van der Hoef, MA.; Ye, M.; van Sint Annaland, M., et al. Computational Fluid Dynamics. Elsevier; 2006.

Verbruggen B, Tóth T, Cornaglia M, et al. Separation of magnetic microparticles in segmented flow using asymmetric splitting regimes. Microfluid Nanofluidics. 2015; 18:91–102.

WHO. Malaria: Report By the Secretariat; Sixty-sixth World Health Assembly. 2013. p. A66/21

Wu W-T, Aubry N, Massoudi M. On the coefficients of the interaction forces in a two-phase flow of a fluid infused with particles. Int J Non Linear Mech. 2014a; 59:76–82.

Wu W-T, Aubry N, Massoudi M, et al. A numerical study of blood flow using mixture theory. Int J Eng Sci. 2014b; 76:56–72. [PubMed: 24791016]

Wu W-T, Yang F, Antaki JF, et al. Study of blood flow in several benchmark micro-channels using a two-fluid approach. Int J Eng Sci. 2015; 95:49–59. [PubMed: 26240438]

Wu X, Wu H, Hu Y. Enhancement of separation efficiency on continuous magnetophoresis by utilizing L/T-shaped microchannels. Microfluid Nanofluidics. 2011; 11:11–24.

Xia N, Hunt TP, Mayers BT, et al. Combined microfluidic-micromagnetic separation of living cells in continuous flow. Biomed Microdevices. 2006; 8:299–308. [PubMed: 17003962]

Yin X, Thomas T, Zhang J. Multiple red blood cell flows through microvascular bifurcations: cell free layer, cell trajectory, and hematocrit separation. Microvasc Res. 2013; 89:47–56. [PubMed: 23727384]

Yung CW, Fiering J, Mueller AJ, Ingber DE. Micromagnetic-microfluidic blood cleansing device. Lab Chip. 2009; 9:1171–1177. [PubMed: 19370233]

Zborowski M, Ostera GR, Moore LR, et al. Red blood cell magnetophoresis. Biophys J. 2003; 84:2638–2645. [PubMed: 12668472]

Zborowski M, Sun L, Moore LR, et al. Continuous cell separation using novel magnetic quadrupole flow sorter. J Magn Magn Mater. 1999; 194:224–230.

Zhang J, Johnson PC, Popel AS. Red blood cell aggregation and dissociation in shear flows simulated by lattice Boltzmann method. J Biomech. 2008; 41:47–55. [PubMed: 17888442]

Zhu T, Lichlyter DJ, Haidekker MA, Mao L. Analytical model of microfluidic transport of non-magnetic particles in ferrofluids under the influence of a permanent magnet. Microfluid Nanofluidics. 2011; 10:1233–1245.

Appendix

Symbol and explanation

Symbol	Explanation	Symbol	Explanation
ρ_p	Density of plasma	$\boldsymbol{\omega}$	Angular velocity
$\boldsymbol{v}_p$	Velocity of plasma	$\tilde{\boldsymbol{F}}^{m,n}_{\text{contact}}$	Tangential component of The contact force
ρ_{p0}	Density of the plasma in the reference configuration	$\tilde{k}$	Tangential spring stiffness
ε	Volume fraction of plasma	$\tilde{\eta}$	Tangential damping coefficient
$\boldsymbol{T}_p$	Constitutive equation of plasma	μ_f	Friction coefficient
p	Pressure of the mixture	$\hat{\boldsymbol{v}}_r^{m,n}$	Relative tangential velocity
λ_p	First coefficients of viscosity of the pure plasma	$\tilde{\delta}$	Tangential displacement
μ_p	Second coefficients of viscosity of the pure plasma	$\boldsymbol{t}^{m,n}$	Tangential unit vector
$\boldsymbol{D}_p$	Symmetric part of the velocity gradient	$\hat{\delta}_0$	Tangential displacement in the previous time step
$\boldsymbol{F}_{pr}$	Interaction forces	$\boldsymbol{n}_0^{m,n}$	Normal direction in the previous time step
$\boldsymbol{b}_p$	Body force	$\boldsymbol{e}_{z'}$	Unit vectors in the z'
m_r	Mass of a RBC	$\boldsymbol{e}_{y'}$	Unit vectors in the y'
$\boldsymbol{x}_r$	Instantial space position of RBCs	μ_w	Magnetic permeability of The ferromagnetic wire
$\boldsymbol{F}_{contact}$	Force of collision with other RBCs or boundaries	μ_0	Magnetic permeability of free space

Symbol	Explanation	Symbol	Explanation
$\boldsymbol{F}_{pr}$	Interaction force with continuous phase	M_s	Saturation magnetization field of the rectangular wire
$\boldsymbol{F}_{ext}$	External force field	χ_p	Magnetic susceptibility of the plasma
$\boldsymbol{F}_{\text{contact}}^{m,n}$	The normal component of the contact force	χ_{rbc}	Magnetic susceptibility of RBCs
$\hat{k}$	Normal "spring" stiffness	V_{rbc}	Volume of the RBCs
$\hat{\eta}$	Normal damping coefficient	a	Nominal radius of the wire
δ	A (fictitious) overlap between two RBCs	H_0	The applied external magnetic field
R	Radius of a RBC	H_c	Constriction height
$\boldsymbol{n}$	Normal unit vector between two RBCs	L_c	Constriction length
$\boldsymbol{v}_r^{m,n}$	Relative velocity	L_d	Diffuser length
$\tilde{\boldsymbol{v}}_r^{m,n}$	Normal relative velocity		

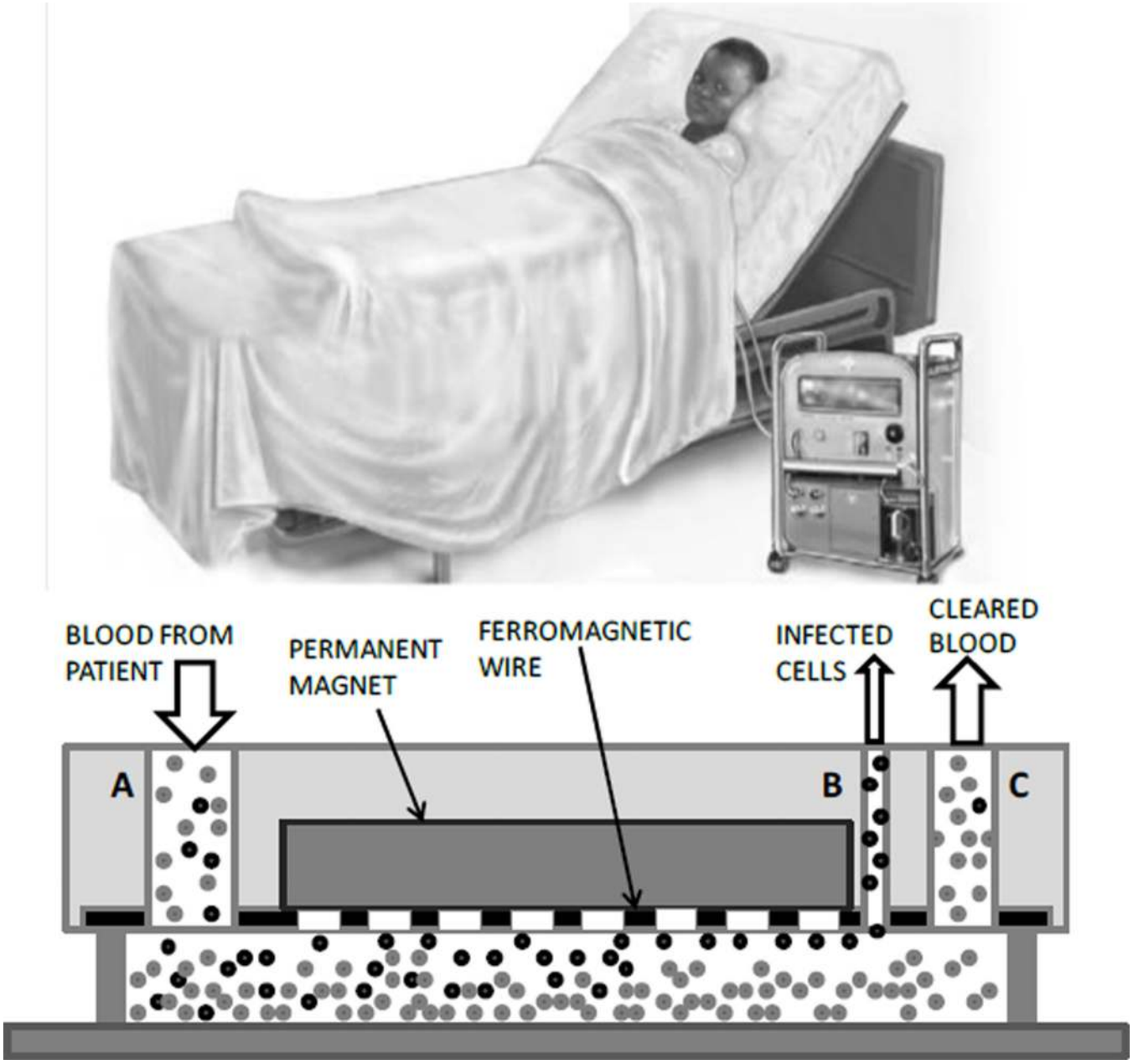

Fig. 1.

The envisioned mPharesis™ system (top) in clinical setting, and (bottom) principle of operation of one of several magnetic separation channels. (A) Blood inlet, (B) Bleed-slit, (C) Return outlet. (Kim et al. 2012)

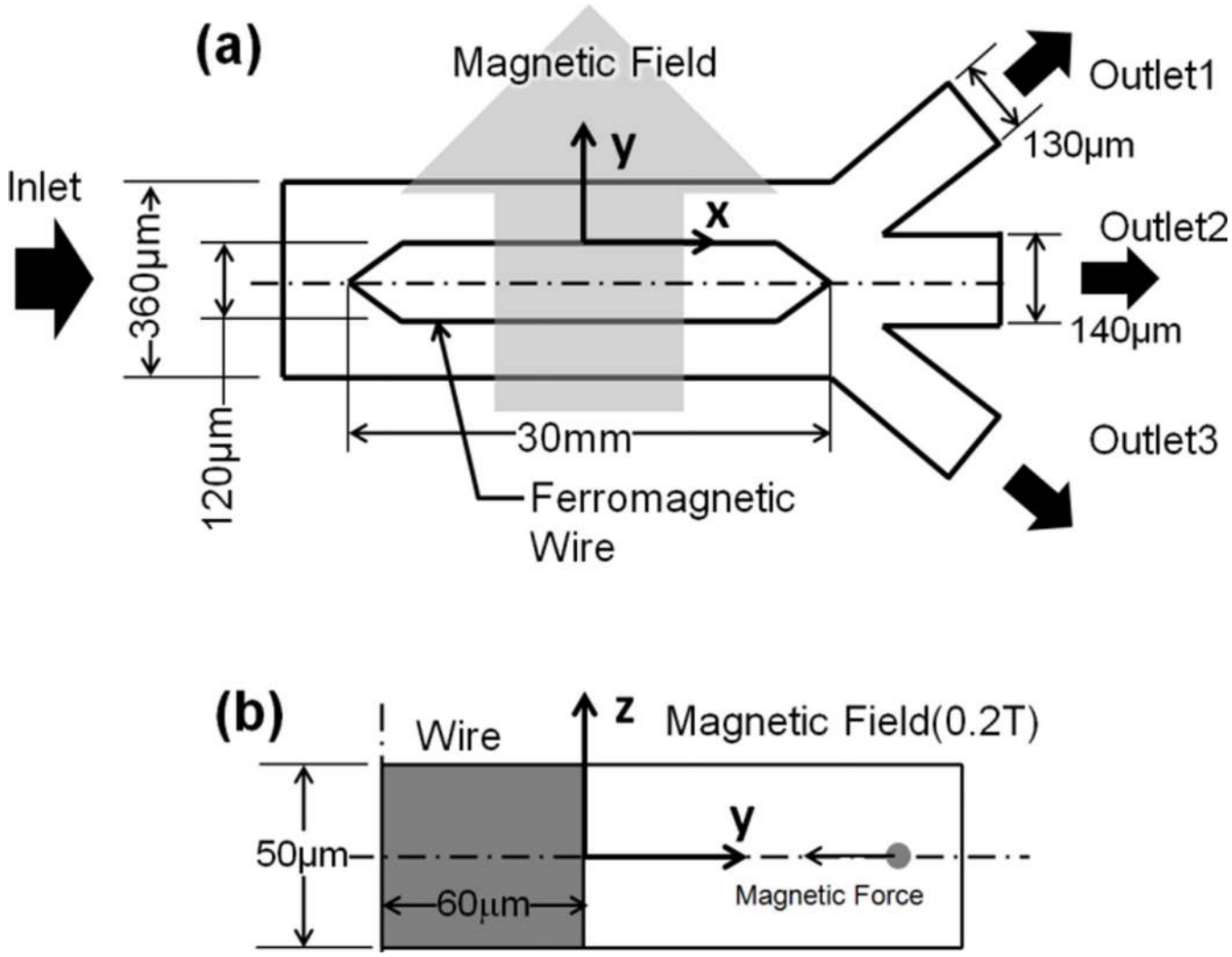

Fig. 2.

Schematic of the magnetophoretic separator with a rectangular ferromagnetic wire. (a) Top view and (b) Cross section view of the microchannel (Han and Frazier 2006).

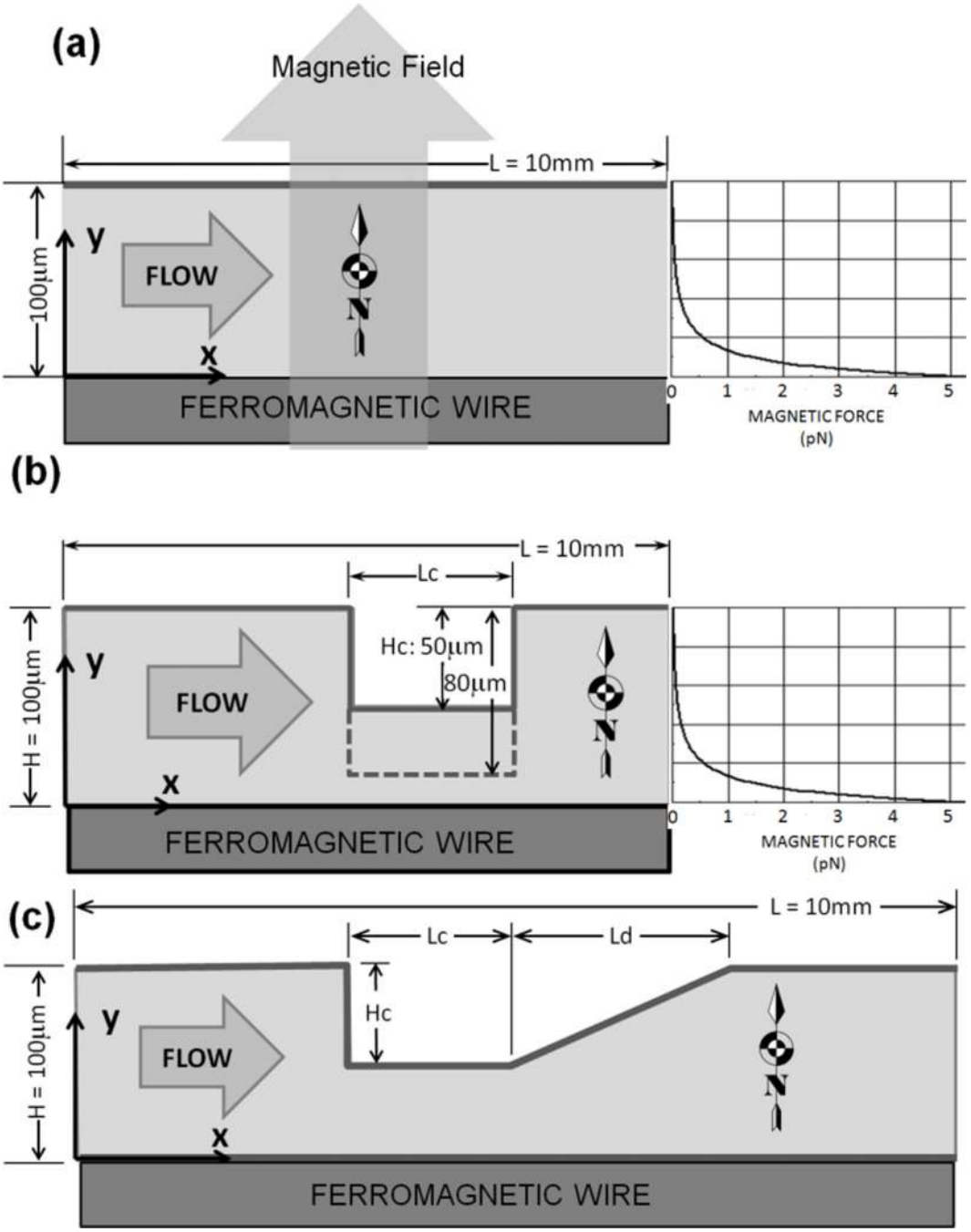

Fig. 3.

Individual separation channel of mPharesis device (not drawn to scale) (a) without constriction; (b) with step constriction; and (c) with constriction and diffuser. For all cases the length of the channels were 10 mm (along × direction) and the entrance/exit height of the channel was 100 µm (along y direction). The simulations were two dimensional therefore there is no dimension along z direction.

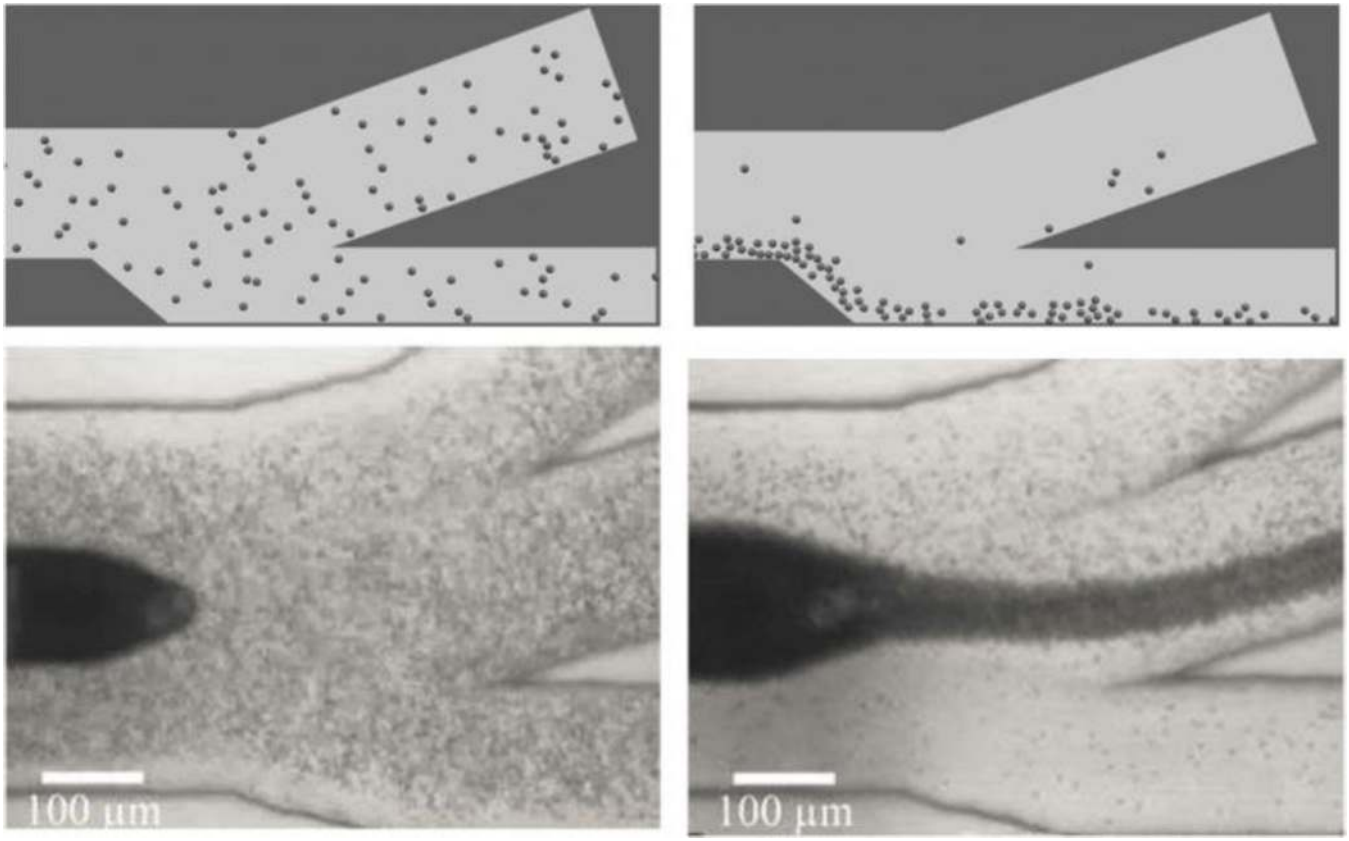

Fig. 4.

Comparison of simulated to experimentally observed deoxyhemoglobin RBCs passing through the microchannel magnetophoretic separator at an average flow velocity of 0.1 mm/s with (left) and without (right) applied magnetic flux (0.2T). Experimental figures were reused with permission (Han and Frazier 2006).

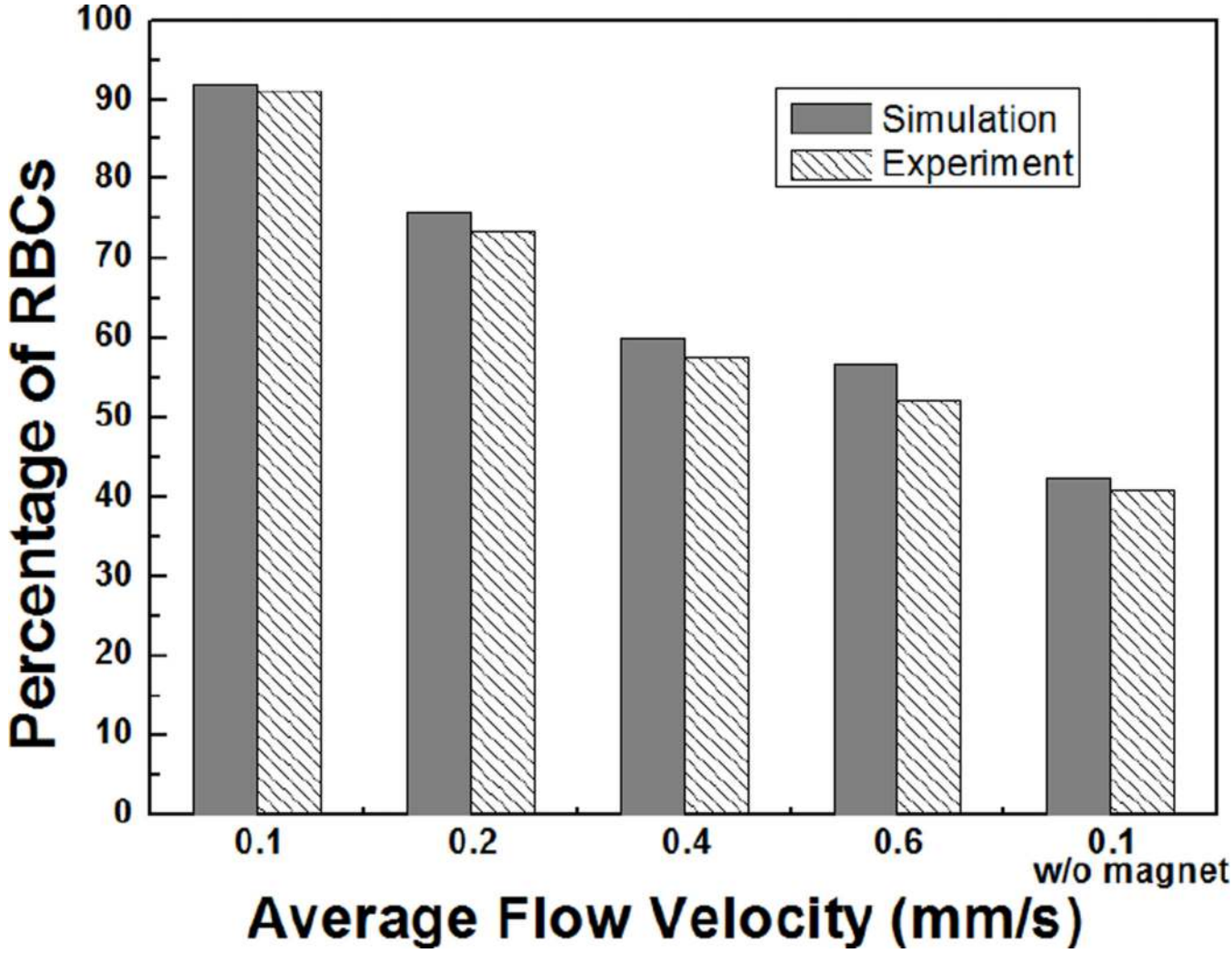

Fig. 5.

Comparison of simulated and experimental separation percentage of deoxyhemoglobin RBCs at outlet2 of the separator for various average flow velocities (Han and Frazier 2006).

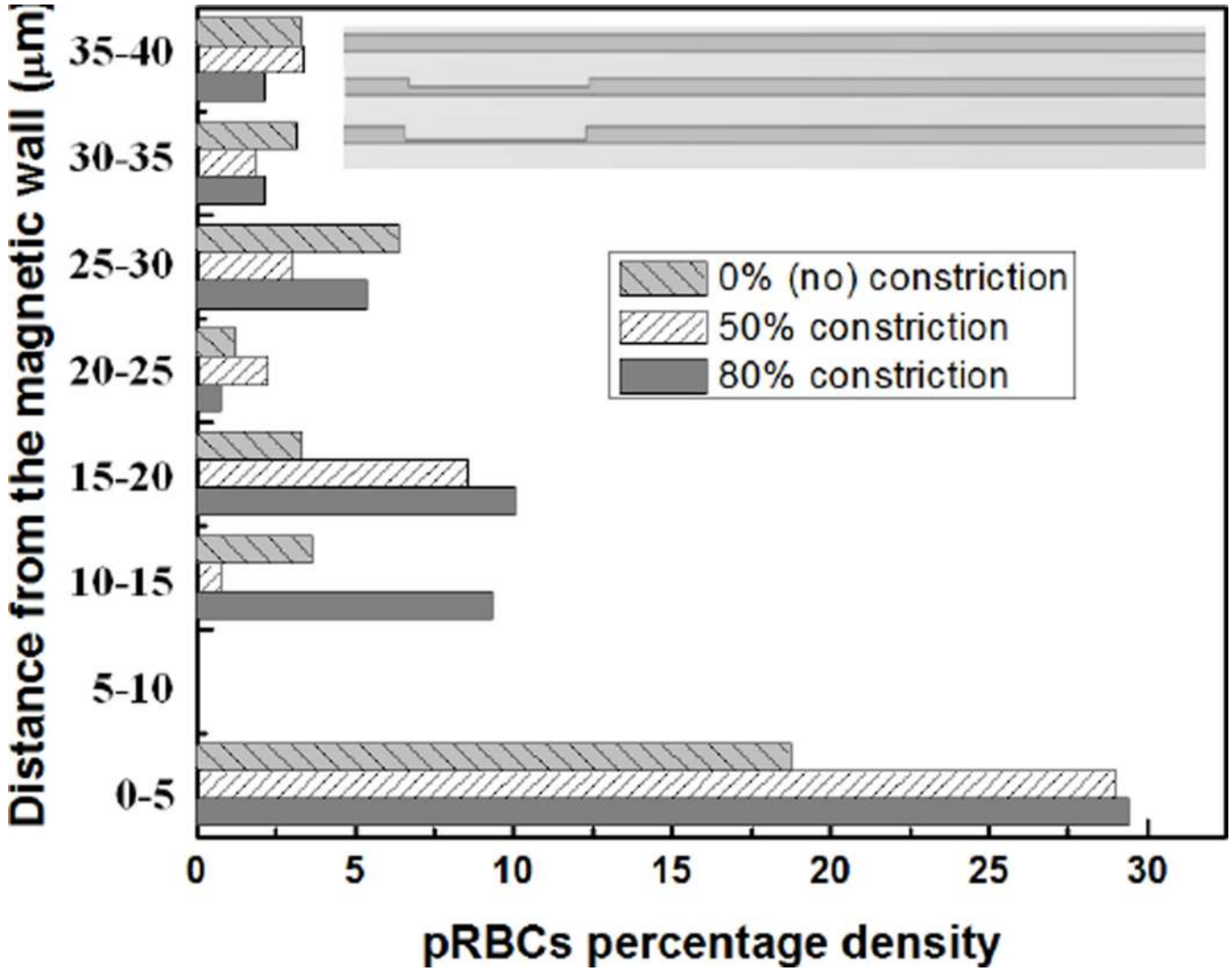

Fig. 6.
Percentage density distribution at the outlet along the y direction, effect of H_c.

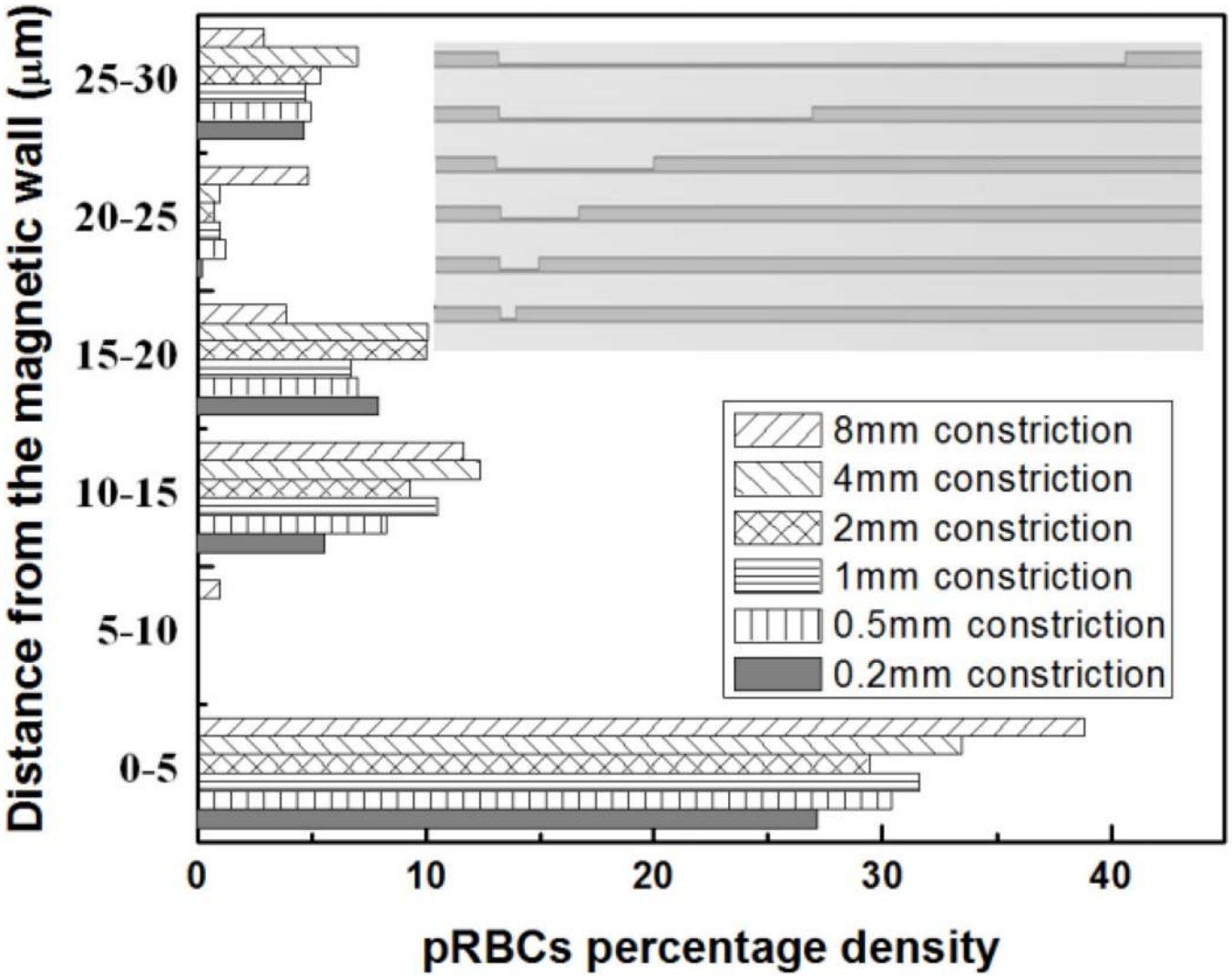

Fig. 7.
Percentage density distribution at the outlet along the y direction, effect of L_c.

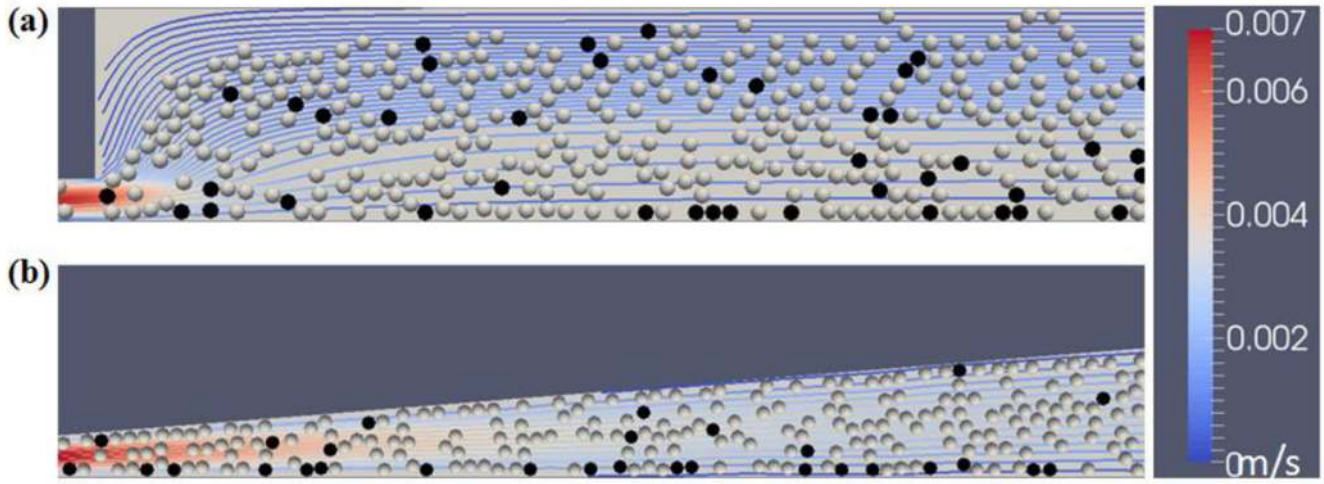

Fig. 8.

Snapshot of RBCs distribution in the channel region near the outlet of the constriction. Black: Infected RBCs; White: Normal RBCs. (a) Channel with H_c = 80 μm, L_c = 2 mm constriction and no diffuser; (b) Channel with H_c = 80 μm, L_c = 2 mm constriction and L_d = 1 mm diffuser.

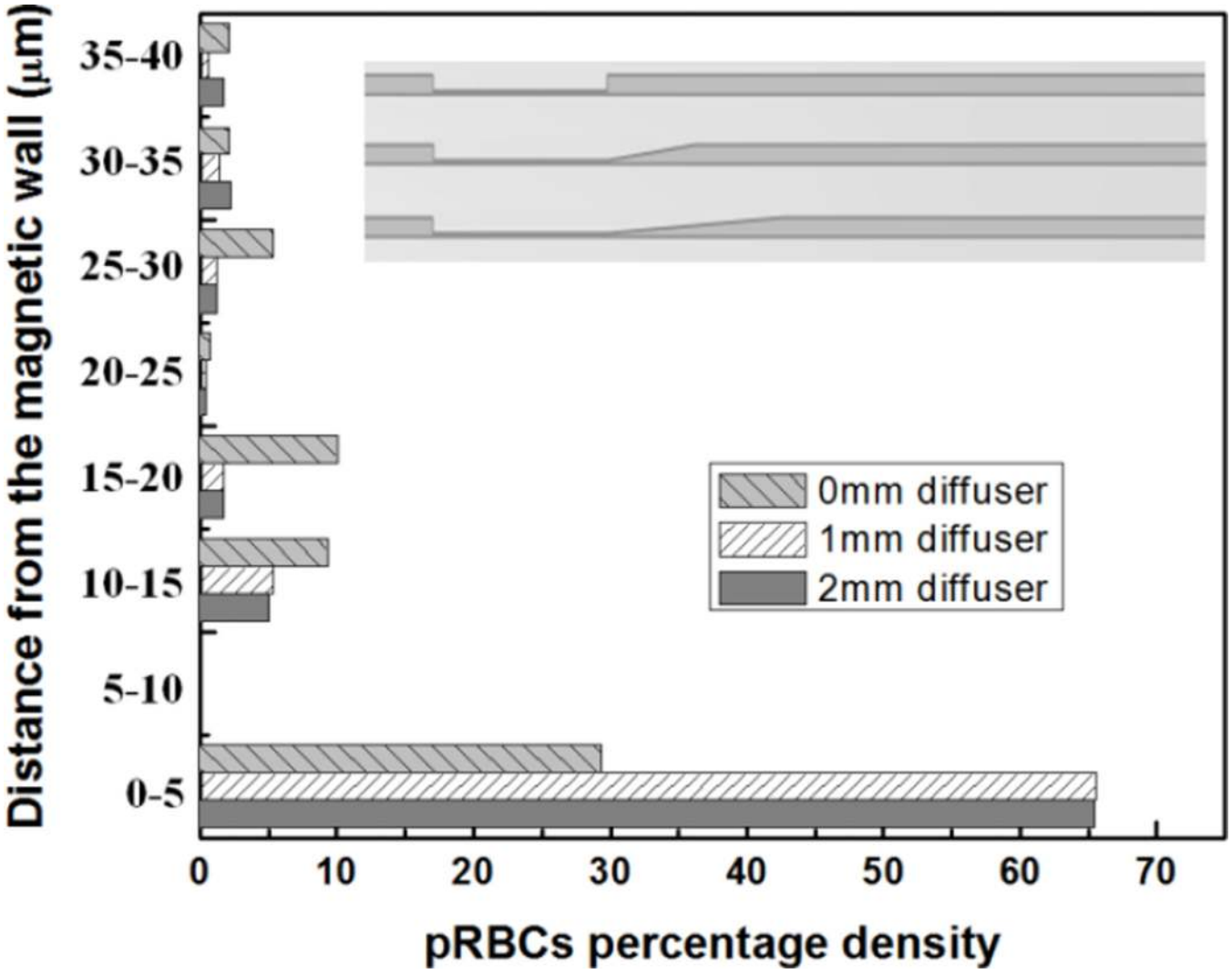

Fig. 9.
Percentage density distribution at the outlet along the y direction, effect of L_d.

Table 1

Physical properties and flow condition. (To economize computational cost the diameter of the RBCs are specified as 8 μm.)

Plasma viscosity	0.96cP
Plasma density	1027 kg/m^3
Diameter of RBCs	8 μ*m*
Young's modules of RBCs	26kPa (Dulińska et al. 2006)
Poisson's ratio of RBCs	0.5 (Dulińska et al. 2006)
Friction coefficient between RBCs and between RBCS and wall	0.08 (Dean et al. 2010)

Table 2

Effect of constriction height on pRBCs separation rate.

Constriction (H_c)	pRBCs Capture	pRBC Enrichment	Δp (Pa)
(No constriction)	26%	28%	17
50% (50 μm)	38%	92%	41
80% (80 μm)	49%	139%	442

Table 3

Effect of constriction length on pRBCs separation rate (H_c = 80 μm).

Length of the constriction (L_c)	pRBCs Capture	pRBC Enrichment	Δ*p* (Pa)
8 mm	55%	177%	1727
4 mm	56%	180%	872
2 mm	49%	139%	442
1 mm	49%	144%	235
0.5 mm	46%	128%	128
0.2 mm	41%	103%	64

Table 4

Effect of diffuser length on pRBCs separation rate (H_c = 80 μm)

Length of the diffuser (L_d)	pRBCs Capture	pRBC Enrichment	Δ*p* (Pa)
none (sudden expansion)	49%	139%	441.94
1 mm	73%	263%	468.20
2 mm	72%	261%	495.91